Micron-particle transport, interactions and deposition in triple lung-airway bifurcations using a novel modeling approach

Y. Feng [a], C. Kleinstreuer [a,b,*]

[a] Department of Mechanical and Aerospace Engineering, North Carolina State University, Raleigh, NC 27695, USA
[b] Joint UNC-NCSU Department of Biomedical Engineering, North Carolina State University, Raleigh, NC 27695, USA

ARTICLE INFO

ABSTRACT

Particulate suspensions inhaled by humans are typically dilute and hence interactions between particles can be neglected. In such cases conventional Euler–Lagrange or Euler–Euler methods are suitable to simulate micron- or nano-particle transport and deposition in human respiratory systems. However, when challenging conditions, such as large pressure differentials, high velocity gradients and/or intense particle collisions, exist, alternative approaches for numerical analysis are required to capture fluid–particle, particle–particle, and particle–wall interactions. In the present study, the dense discrete phase model (DDPM) in conjunction with the discrete element method (DEM) have been employed to simulate micron–particle transport, interaction and deposition dynamics in different triple bifurcations (i.e., G3–G6, G6–G9, and G9–G12), using ANSYS Fluent 14.0 enhanced by user-defined functions (UDFs). In light of the relatively high computational cost when employing DDPM–DEM for such simulations throughout the human respiratory system, it may be necessary to combine different computational fluid–particle dynamics (CF–PD) models based on the *local intensity* of particle–particle interactions. Thus, the validity and necessity of the DDPM–DEM approach for different lung airway generations were numerically investigated, considering new parametric criteria for the use of most suitable numerical models. Specifically, the relative intensities of three major particle deposition mechanisms (i.e., inertial impaction, secondary-flow effect, and particle–particle-interaction impact) in idealized lung-airway segments were investigated. As a result, a new criterion for CF–PD model combination in terms of a relationship between inlet-particle stacking-volume fraction, ϕ, and percentage-of-fate changing particles, $\Delta\beta_p$, is proposed. Visualizations of the fluid–particle dynamics in bifurcating airways have been provided as well. Results of this study pave the way for accurate and cost-effective CF–PD simulations of lung-aerosol dynamics, aiming at the improvement of respiratory dose estimation for health risk assessment in case of toxic particles and for treatment options in case of therapeutic particles.

1. Introduction

Accurate simulation of airflow structures and related aerosol deposition in realistic models of the human respiratory system, using computational fluid–particle dynamics (CF–PD), are of fundamental importance (Kleinstreuer & Feng, 2013).

---

* Corresponding author at: Department of Mechanical and Aerospace Engineering, North Carolina State University, Raleigh, NC 27695, USA.
Tel.: +1 919 515 5216; fax: +1 919 515 7968.
E-mail address: ck@ncsu.edu (C. Kleinstreuer).

Nomenclature

$d_{p,eq}$	equivalent particle diameter	$\vec{v}_{pn,ij}$	normal component of the relative velocity $\vec{v}_{p,ij}$ between particle i and particle j
d_p	particle diameter	$\vec{v}_{pt,ij}$	tangential component of the relative velocity vector between particle i and particle j
D_{in}	inlet diameter		
DE	deposition efficiency		
E_{eq}	equivalent Young's modulus	*Greeks*	
$\vec{F}_{c,ij}$	inter-particle contact force between particle i and particle j	α_f	fluid volume fraction
$\vec{F}_{c,ij}^{\,n}$	normal contact force between particle i and particle j	$\Delta\beta_p$	percentage of fate changing particles
		δ	unit tensor
$\vec{F}_{c,ij}^{\,t}$	tangential contact force between particle i and particle j	δ_{nij}	normal overlap distance between contacting particle i and particle j
$\vec{F}_{D,i}$	drag force acting on particle i	ε	the coefficient of restitution
$\vec{F}_{pf,i}$	fluid–particle interaction forces acting on particle i	η_{nij}	normal damping coefficient
		σ	Poisson's ratio
$\vec{F}_{g,i}$	the gravity of particle i	$\vec{\tau}_f$	local stress tensor
G	the particle's shear modulus	ϕ	inlet particle stacking volume fraction
k_n	normal stiffness		
k_v	the number of particles in the specific mesh cell	*Subscripts and superscripts*	
M_{layer}	initial stacking-layer number of particles	c	contact force
N_{in}	the total number of particles released at the inlet	f	fluid phase
		i	particle index i
$\vec{R}_{sl}$	volumetric fluid–particle interaction force	in	inlet
Re_{in}	inlet Reynolds number	j	particle index j
St	Stokes number	n	normal direction
Δt_p	discrete-phase time step	p	particulate phase
		t	tangential direction

For the inhalation of micron particles, most will typically deposit before passing through the trachea due to inertial impaction and strong turbulent dispersion in the oral region and nasal cavities. The remaining particle suspension is dilute when entering the tracheobronchial airways so that particle–particle interacting mechanisms can be neglected. In such cases conventional Euler–Lagrange methods are accurate for the prediction of particle transport and deposition in lung airways. However, when high concentrations of air pollutants are inhaled or dense drug particle suspensions are delivered for lung or systemic disease targeting, particle–particle and particle–wall interactions are the dominant features which strongly influence particle transport and deposition in lung airways (Aljuri et al., 2012; Kleinstreuer et al., 2008; Tong et al., 2010). Conventional Euler–Lagrange methods (i.e., discrete phase models (DPMs)) are not suitable for dense fluid–particle flows because of the restriction on the volume fraction of the discrete phase. Such numerical DPMs do not consider explicitly the contact between the fluid, particles and wall surfaces with respect to particle inertial and material properties. Additionally, two-way coupling is necessary for dense particle-suspension flows in complex conduits. The use of the discrete element method (DEM) will ensure realistic particle flow. It was first proposed by Cundall & Strack (1979), based on molecular dynamics. The most attractive feature of DEMs is the highly efficient algorithms of the contact detection and contact force calculation between arbitrary shaped particles (Wang et al., 2010). The dense discrete phase model (DDPM) combined with DEM is one of the CF–PD modeling approaches discussed by Tsuji et al. (1992, 1993). Specifically, with CFD–DEM which is similar to DDPM–DEM, the motion of translating and interacting particles is described by DEM, based on Newton's second law, while the DDPM describes the fluid flow field, determined by a solution of the local averaged Navier–Stokes equations. The coupling between the discrete and continuous phases can be achieved via an interphase interaction term in the Navier–Stokes equation (Kafui et al., 2002). Thus, in DDPM–DEM the motion of each particle is analyzed by incorporating the contact forces and the moments due to the neighboring particles. This method has gained a prominent application in the modeling of fluidized beds (Alobaid et al., 2012; Li et al., 2012; Neuwirth et al., 2012), as well as multi-scale strategy achievement which combines different numerical models that describe gas–solid flows at different levels of detail (e.g., DNS, DEM, and DPM) (Di Renzo et al., 2011; Van der Hoef et al., 2008). The coupling algorithm of DDPM–DEM is presented by Fig. 1. More recent applications include the investigation of dense powder dispersion in drug-aerosol inhalers (Tong et al., 2010, 2012), as well as pulmonary drug delivery, as discussed by Chen et al. (2012). Specifically, its application to inhaler development has largely been focused on investigating pharmaceutical agglomerate break-up in dry powder inhalers (Wong et al., 2012). For example, Tong et al. (2010, 2012) recently employed ANSYS Fluent with in-house user-defined functions (UDFs) to powder dispersion in a commercial Aerolizer® Inhaler model. Chen et al. (2012) employed the one-way and two-way DDPM–DEM methods for particle transport and deposition in a pulmonary airway bifurcation. They
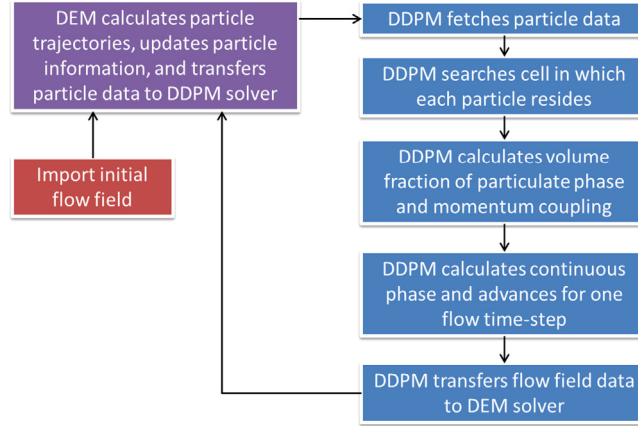
Fig. 1. Coupling and information exchange between DDPM solver and DEM solver.

validated the DDPM–DEM method by deposition-efficiency comparisons between their numerical results and experimental data (Kim & Fisher, 1999) in Weibel's double bifurcation airway geometry (G3–G5), using spherical micron particles with diameters ranging from 3 μm to 7 μm. However, the particulate inlet volume fraction they assumed was below 1.85% (i.e., 10,000 particles with $d_p = 10$ μm generated near the inlet), a situation where particle–particle interactions are actually negligible. Hence, the application of DDPM–DEM with two-way coupling for dense particle suspension flow has not been systematically investigated.

Because DDPM–DEM is a computationally taxing method to apply, especially for lung aerosol dynamics simulations (Feng, 2013), it is desirable to reduce the CPU cost. For example, by resorting to other numerical approaches when appropriate, e.g., conventional Euler–Lagrange methods at locations with low particle–volume fractions. This, however, will require a criterion when and where to combine the different models for accurate and effective simulations.

In this paper, DDPM–DEM was developed and employed for the simulation of particle transport and deposition in different bifurcating airways. Focusing on laminar, incompressible flow, the time evolution of particle transport, the resulting deposition efficiencies, and particle transport patterns were investigated. Specifically, the two-way DDPM–DEM, one-way DPM, and two-way DPM were used to simulate particulate suspensions in different triple-bifurcation lung airway geometries (i.e., G3–G6, G6–G9, and G9–G12) for mouth inlet flow rates of 30 L/min and 60 L/min. Parametric impact analyses on particle transport and deposition patterns were investigated as a function Stokes number, inlet Reynolds number, and particle-to-inlet-diameter ratio, d_p/D_{in}. In addition, a criterion for judging the necessity of employing DDPM–DEM rather than just DPM was introduced for the triple-bifurcation airways, representing different generations.

2. Theory

2.1. Governing equations for the continuous phase (DDPM)

For gas–solid two-phase flow, the governing equations for the continuous phase in the DDPM–DEM method are conservation of mass and momentum of the local mean variables over a cell, which can be written as follows (Johnson, 1998; Loth, 2008).

Continuity equation:

$$\frac{\partial(\alpha_f \rho_f)}{\partial t} + \nabla \cdot (\alpha_f \rho_f \overrightarrow{v_f}) = 0 \tag{1}$$

and
Momentum equation:

$$\frac{\partial(\rho_f \alpha_f \overrightarrow{v_f})}{\partial t} + \nabla \cdot (\alpha_f \rho_f \overrightarrow{v_f} \cdot \overrightarrow{v_f}) = -\alpha_f \nabla p + \nabla \cdot (\alpha_f \overrightarrow{\tau}_f) + \alpha_f \rho_f \overrightarrow{g} - \overrightarrow{R_{sl}} \tag{2}$$

Here, α_f is the fluid volume fraction and $\overrightarrow{\tau}_f$ is the local stress tensor given by Hilton & Cleary (2011) as

$$\overrightarrow{\tau}_f = \mu_f \left(\nabla \overrightarrow{v_f} + \nabla \overrightarrow{v_f}^{tr} - \left(\frac{2}{3} \nabla \cdot \overrightarrow{v_f} \right) \delta \right) \tag{3}$$

where δ is the unit tensor. In Eq. (2) $\overrightarrow{R_{sl}}$ is the volumetric fluid–particle interaction force. The "averaged-discrete-phase-drag" method can be employed to calculate $\overrightarrow{R_{sl}}$ as

$$\overrightarrow{R_{sl}} = \frac{\sum_{i=1}^{k_v} \overrightarrow{F}_{D,i}}{\Delta V} \tag{4}$$

where index k_v is the number of particles in the specific mesh cell, ΔV is the volume of the current mesh cell, and $\overrightarrow{F}_{D,i}$ is the drag force acting on particle i.

2.2. Translational equation for the discrete phase (DEM)

In this study, only translational motion of the dense particulate discrete phase was considered:

$$m_{p,i}\frac{d\overrightarrow{v}_{p,i}}{dt} = \sum_j \overrightarrow{F}_{c,ij} + \overrightarrow{F}_{pf,i} + \overrightarrow{F}_{g,i} \tag{5}$$

where $\overrightarrow{F}_{c,ij}$ are the inter-particle contact forces, $\overrightarrow{F}_{pf,i}$ are fluid–particle interaction forces acting on particle i, and $\overrightarrow{F}_{g,i}$ is the gravity of particle i. Specifically, particle–particle contact and interaction schematics are shown in Fig. 2(a) and (b).

$$\overrightarrow{F}_{c,ij} = \overrightarrow{F}_{c,ij}^{n} + \overrightarrow{F}_{c,ij}^{t} \tag{6}$$

$$\overrightarrow{F}_{pf,i} = \overrightarrow{F}_{D,i} \tag{7}$$

Here, $\overrightarrow{F}_{c,ij}^{n}$ and $\overrightarrow{F}_{c,ij}^{t}$ are the normal and tangential contact forces between particles i and j; and $\overrightarrow{F}_{D,i}$ is the drag force acting on particle i. Proper models and expressions for $\overrightarrow{F}_{c,ij}^{n}$, $\overrightarrow{F}_{c,ij}^{t}$, and $\overrightarrow{F}_{D,i}$ were selected to achieve simulation accuracy and computational economy.

2.2.1. Normal contact force

The Hertz–Mindlin no-slip model (see Fig. 2(b)) was employed for modeling the normal contact force (Crowe et al., 2011; Ren et al., 2011). Describing particle contacts as damped harmonic oscillators, the contact force can be expressed as

$$\overrightarrow{F}_{c,ij}^{n} = \overrightarrow{F}_{cn,ij} + \overrightarrow{F}_{dn,ij} \tag{8}$$
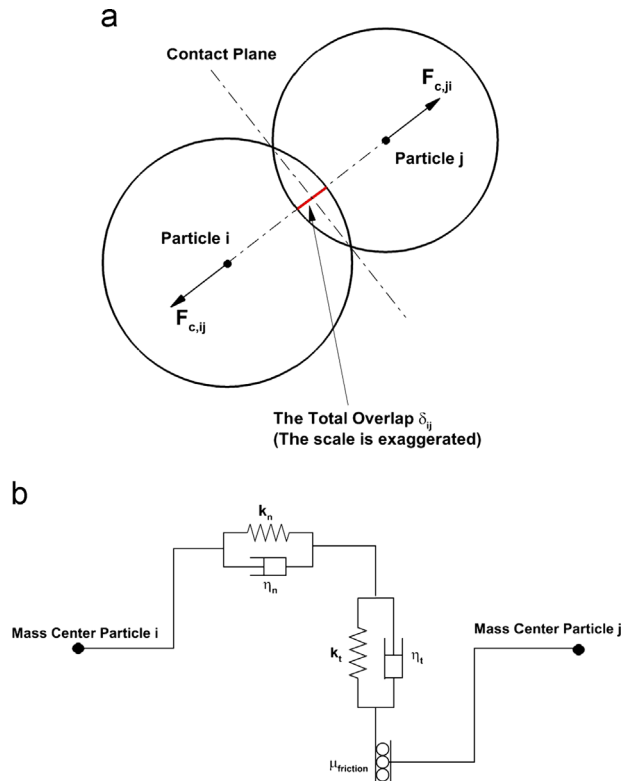

Fig. 2. Particle–particle interaction diagrams: (a) particle–particle contact overlap; (b) sketch of simplified Hertz–Mindlin contact model.

where

$$\overrightarrow{F}_{cn,ij} = -k_n \delta_{nij}^{3/2} \overrightarrow{n}_{ij} \tag{9}$$

and

$$\overrightarrow{F}_{dn,ij} = -\eta_{nij} \overrightarrow{v}_{pn,ij} \tag{10}$$

In Eq. (9), δ_{nij} is the normal overlap distance between contacting particle i and particle j; k_n is the normal stiffness which can be expressed, based on Hertzian contact theory, as

$$k_n = \frac{4}{3} E_{eq} \sqrt{\frac{d_{p,eq}}{2}} \tag{11}$$

Here, E_{eq} is the equivalent Young's modulus and $d_{p,eq}$ is the equivalent particle diameter. The two parameters are defined as

$$E_{eq} = \left(\frac{1-\sigma_i^2}{E_i} + \frac{1-\sigma_j^2}{E_j} \right)^{-1} \tag{12}$$

and

$$d_{p,eq} = \left(\frac{d_{p,i}+d_{p,j}}{2d_{p,i}d_{p,j}} \right)^{-1} \tag{13}$$

in which σ is Poisson's ratio.

In Eq. (10), η_{nij} is the normal damping coefficient which can be given by a revised correlation of Raji (1999). It is based on the analytical relationship between the normal damping coefficient η_{nij} and the coefficient of restitution ε ($0 \le \varepsilon \le 1$) (Crowe et al., 2011; Tsuji et al., 1993):

$$\eta_{nij} = -\frac{\sqrt{5} \ln \varepsilon}{\sqrt{\pi^2 + \ln^2 \varepsilon}} \sqrt{m_{eq} k_n} \delta_{nij}^{1/4} \tag{14}$$

where m_{eq} is the equivalent particle mass:

$$m_{eq} = \left(\frac{1}{m_{p,i}} + \frac{1}{m_{p,j}} \right)^{-1} \tag{15}$$

$\overrightarrow{v}_{pn,ij}$ is the normal component of the relative velocity $\overrightarrow{v}_{p,ij}$ between particle i and particle j. $\overrightarrow{v}_{pn,ij}$ is defined as

$$\overrightarrow{v}_{pn,ij} = (\overrightarrow{v}_{p,ij} \cdot \overrightarrow{n}_{ij}) \overrightarrow{n}_{ij} \tag{16}$$

where $\overrightarrow{v}_{p,ij}$ is defined as

$$\overrightarrow{v}_{p,ij} = \overrightarrow{v}_{p,j} - \overrightarrow{v}_{p,i} \tag{17}$$

2.2.2. Tangential contact force

The friction collision law was used for modeling the tangential contact force which is based on the Coulomb friction law (Feng, 2013), i.e.,

$$\overrightarrow{F}_{c,ij}^{t} = \mu_{friction} \left| \overrightarrow{F}_{c,ij}^{n} \right| \frac{\overrightarrow{v}_{pt,ij}}{|\overrightarrow{v}_{pt,ij}|} \tag{18}$$

where $\overrightarrow{v}_{pt,ij}$ is the tangential component of the relative velocity vector between particle i and particle j; $\overrightarrow{v}_{pt,ij}$ is defined as

$$\overrightarrow{v}_{pt,ij} = (\overrightarrow{v}_{p,ij} \times \overrightarrow{n}_{ij}) \times \overrightarrow{n}_{ij} = \overrightarrow{v}_{p,ij} - \overrightarrow{v}_{pn,ij} \tag{19a, b}$$

The friction coefficient $\mu_{friction}$ is related to the magnitude of the relative tangential velocity vector $|\overrightarrow{v}_{pt,ij}|$ (Armstrong & de Wit, 1996).

2.2.3. Drag force

For spherical particle i, the drag force "uniform Newtonian fluid flow" can be expressed as

$$\overrightarrow{F}_{D,i} = \frac{1}{2} C_D \frac{\pi d_{p,i}^2}{4} \rho_f (\overrightarrow{v}_{p,i} - \overrightarrow{v}_f) |\overrightarrow{v}_{p,i} - \overrightarrow{v}_f| \tag{20}$$

where for the drag coefficient the combination of Ergun (1952) and Wen & Yu (1966) has been widely used. In the present study for micron particles, the drag coefficient is

$$
C_D = \begin{cases} \dfrac{24}{\text{Re}_p} & \alpha_f \text{Re}_p < 0.5 \\ \dfrac{24}{\alpha_f \text{Re}_p}(1 + 0.15\alpha_f^{0.687}\text{Re}_p^{0.687}) & 0.5 < \alpha_f \text{Re}_p < 1000 \\ 0.44 & \alpha_f \text{Re}_p > 1000 \end{cases}
\tag{21}
$$

$$
\text{Re}_p = \frac{\rho_f |\overrightarrow{v}_f - \overrightarrow{v}_p| d_p}{\mu_f}
\tag{22}
$$

It is worth mentioning that for micron particles with $d_p \geq 10\ \mu\text{m}$, the Cunningham correction factor is negligible.

2.3. Geometry and mesh

A representative triple bifurcation bronchial airway model was selected for this study (see Fig. 3(a) and (b)). The dimensions of the triple bifurcating geometry are representative for adults with a lung volume of 3500 mL. To represent bifurcating airways starting from different generations, the triple bifurcating airway geometry was scaled to duplicate the hydraulic diameter D_1 of the first bifurcation of different generations. For example, $D_1 = 0.6$ cm represents the G3–G6 bifurcating lung airways, while $D_1 = 0.026$ cm represents the G6–G9 bifurcating lung airways, etc.

For the numerical simulation a structured, multi-block, body-fitted hexahedral mesh was developed (see Fig. 3(b)). Mesh independence tests have been successfully executed and presented in published papers (e.g., Zhang & Kleinstreuer, 2001). The final mesh contained 628,712 cells, 655,822 nodes, and 1,912,466 faces.
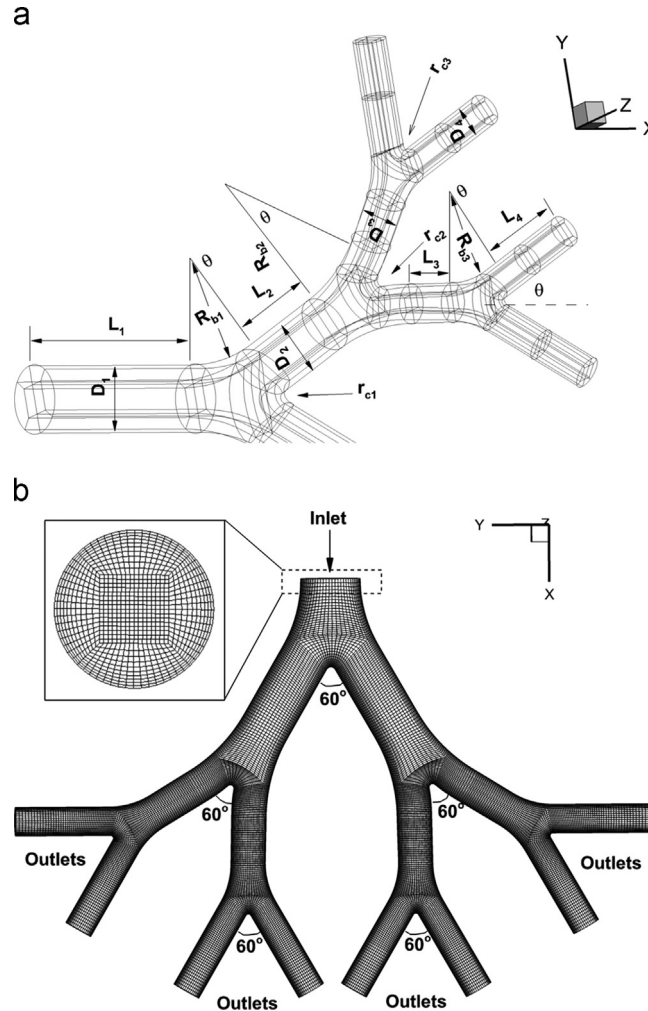

Fig. 3. (a) Geometry and block structure of Weibel's triple bifurcation geometry; (b) finite volume mesh.

2.4. Boundary conditions

2.4.1. Parabolic inlet velocity

To avoid entrance effects for numerical model validation, a fully-developed (parabolic) velocity was employed at the inlet, which was created via an in-house user-defined function (UDF) program (Feng, 2013). The averaged inlet velocity was determined from inhalation flow rates at the mouth, i.e., either 30 L/min or 60 L/min. To facilitate the determination of inlet conditions, two assumptions were introduced:

(1) The lung morphology is identical to the idealized model proposed by Weibel (1963).
(2) Mass flow rate in each branch at the same generation is evenly distributed.

2.4.2. Random-parabolic particle injection

In order to approximate realistic particle-inlet conditions (Kim & Fisher, 1999), a random-parabolic particle distribution was used at the inlet. Specifically, particle position generation was achieved via an in-house Matlab code with which particles are placed randomly (Feng, 2013). When employing DDPM–DEM, to avoid artificial initial contact forces between particles, a re-alignment mechanism was activated during the particle generation process. For example, if the initially assigned position of the particle would cause an overlap with any other physical element in the flow domain (i.e., other particles or boundaries), the code will abandon the position and try to assign another one. The maximum number of attempts to place a particle was 20. The effective particle diameter ranged from 4 μm to 10 μm. The particle density varied with the Stokes number, which ranged from 0.037 to 0.125. In order to have dilute as well as dense particle suspension flows, the inlet particle stacking volume fraction was changed from 2% to 30%.

2.4.3. Ideal particle-trapping wall and uniform pressure outlets

The particle–wall interaction boundary condition was assumed to be a "100% trapped wall", because of the existence of mucus layers which coat the inner wall of lung airways. Also, uniform (zero) gage pressure was applied at the terminal outlets.

2.5. Validity and necessity of DDPM–DEM in airway bifurcations

The potential computational cost of DDPM–DEM is very high (see Table 1). Clearly, using two-way DDPM–DEM requires much more CPU time (i.e., O(10)–O(1000)) when compared to one-way DPM or two-way DPM. Hence, for future nano/micron-particle transport and deposition simulations when considering the whole human respiratory system, the validity and necessity of DDPM–DEM combined CF–PD models need to be evaluated. Furthermore, to establish criteria for the model combination between DDPM–DEM and DPM, it is essential to investigate the predicted differences of DE between using DDPM–DEM and DPM, and find out factors which have a significant impact on the DE differences.

The deposition efficiency (DE) is a function of six variables:

$$DE = f(\rho_p, d_p, D_{in}, \overline{V_{in}}, N_{in}, M_{layer}) \tag{24}$$

where N_{in} is the total number of particles released at the inlet and M_{layer} is the initial stacking layer number of the particles. Using Buckingham's pi-theorem, three independent dimensionless parameters can be proposed to replace the six variables which then represent the DE's functional relationship. Those dimensionless parameters are introduced for quantitative analyses and for choosing different two-phase modeling approaches (i.e., DDPM–DEM, DPM, etc.). Specifically, the three dimensionless parameters are the Stokes number, the airflow inlet Reynolds number, and a newly defined particle-phase parameter ϕ (initial fluidized bed voidage is $1 - \phi$). The inlet particle stacking volume fraction (PSVF) ϕ is given by

$$\phi = \frac{2N_{in}d_p^2}{3M_{layer}D_{in}^2} \tag{25}$$

Hence, Eq. (24) can be rewritten as

$$DE = f(\text{Re}_{in}, \text{St}, \phi) \tag{26}$$

Table 1
Computational single-CPU time (in hour) comparisons between one-way DPM, two-way DPM, and DDPM–DEM for selected cases in the G6–G9 geometry ($\text{Re}_{in} = 1000$, $0.037 \leq \text{St} \leq 0.125$, number of particle released $= 10,000$).

	St=0.037	St=0.067	St=0.095	St=0.125
1-way DPM	0.064	0.061	0.060	0.060
2-way DPM	6.26	4.87	3.98	3.59
DDPM–DEM	109.34	90.52	79.67	74.76

Furthermore, the percentage of fate changing particles (PFCP), $\Delta\beta_p$, is introduced as the quantity to evaluate the impact of different numerical methods on the deposition efficiency. The PFCP is defined as

$$\Delta\beta_p = \frac{N_{dep,DEM} - N_{dep,DPM}}{N_{in}} \tag{27}$$

where $N_{dep,DEM}$ is the number of deposited particles using DDPM–DEM, and $N_{dep,DPM}$ is the deposited particle number using DPM.

2.6. Numerical setup

The coupling algorithm of DDPM–DEM considering particle–particle interactions has been documented by Feng (2013). The governing equations, subject to appropriate boundary conditions, were numerically solved by a commercial finite-volume based program, i.e., ANSYS Fluent 14.0 (ANSYS Inc., Canonsburg, PA) enhanced by in-house user-defined functions (UDFs). The numerical simulations were performed on a local Dell Precision T3500 workstation with 12 GB RAM and four 3.33 GHz CPUs as well as a local Dell Precision T7500 workstation with 40 GB RAM and twelve 3.33 GHZ CPUs. The typical single-processor running time of two-way coupling DDPM–DEM for fluid flow and particle transport under steady-state inlet conditions lasted from 72 to 168 h, when considering different inlet Reynolds numbers and different triple bifurcation geometries.

In the present study, the discrete-phase time step Δt_p was set smaller than 50% of the characteristic time τ_c (i.e., the Rayleigh time) that corresponds to a typical contact time between colliding particles (O'Sullivan & Bray, 2004), i.e.,

$$\Delta t_p \leq 0.5\tau_c = \frac{0.5\pi r_p}{0.163\sigma + 0.877} \sqrt{\frac{\rho_p}{G}} \tag{28}$$

where G is the particle shear modulus, and σ is the Poisson's ratio. The physical and numerical parameters for particle–particle interactions were identical to those selected by Chen et al. (2012). Laminar flow was assumed since Reynolds number is less than 2000 from G3 to G12 when the mouth inlet flow rate is less than 60 L/min.

3. Model validations and comparisons

Currently no experimental data sets are available for the dynamics of dense micron particulate suspensions in bifurcating lung airways. Besides, only one journal paper (Chen et al., 2012) published before this study applied DDPM–DEM method in lung aerosol dynamics research. Therefore, it is also necessary to see the importance of particle–particle interactions on particle deposition efficiencies in both dilute and dense particle suspensions. Hence for DDPM–DEM model validations, experimental data of Kim & Fisher (1999) as well as numerical simulation results of Chen et al. (2012) for micron-particle deposition in G3–G6 airways from *dilute particle suspensions* were employed. Figure 4(a) and (b) show that the deposition efficiency (DE) is an exponential function of the Stokes number, which coincides with published observations (e.g., Comer et al., 2000; Zhang & Kleinstreuer, 2001). The relatively small differences between experimental data (Kim & Fisher, 1999) and the present numerical study can be attributed to:

(1) experimental uncertainties;
(2) small discrepancies between the computational geometry (Zhang & Kleinstreuer, 2001) and experimental glass tube model (Kim & Fisher, 1999);
(3) higher experimental DE, induced by turbulent flow regime, as the experimental Reynolds number range was 283–4718, which extended to turbulent airflow; and
(4) exclusion of the coagulation effect on DE in the present numerical simulation studies.

Compared with our numerical simulation results using one-way DPM and two-way DPM, DDPM–DEM predicted slightly lower DE-values in the 1st bifurcation and 2nd bifurcation. The possible explanation is that the particle–particle contact forces provide accelerations to some particles, avoiding impaction and/or sedimentation. A similar discovery was reported by Cui (2012), who mentioned that using a two-way coupling method provides lower deposition efficiencies of sub-micron and micron particles compared to one-way DPMs. It can be also observed that the predicted "DE difference" between DDPM–DEM and DPM becomes more noticeable when the Stokes number increases (see Fig. 4(a) and (b)). This is because a higher Stokes number indicates a greater ability of particles to cross laminar flow layers and collide with other particles. Thus, at higher Stokes numbers more particles will be influenced by particle–particle interactions, leading via the use of DDPM–DEM to different results when compared to using DPM (i.e., the basic Euler–Lagrange approach).

Not surprising, numerical results based on either DDPM–DEM or DPM show a good agreement with each other (see Fig. 4(a) and (b)). Specifically, with the maximum particulate volume fraction of just 1.85%, the discrete phase is dilute, and hence any particle–particle interaction frequency should be extremely low. Therefore, DDPM–DEM and DPM should provide very similar DE distributions in G3–G6. Nevertheless, for the second bifurcation (Fig. 4(b)), measurable differences in DE-values appear for St > 0.08 when employing DDPM–DEM due to increased occurrences of particle–particle interaction.
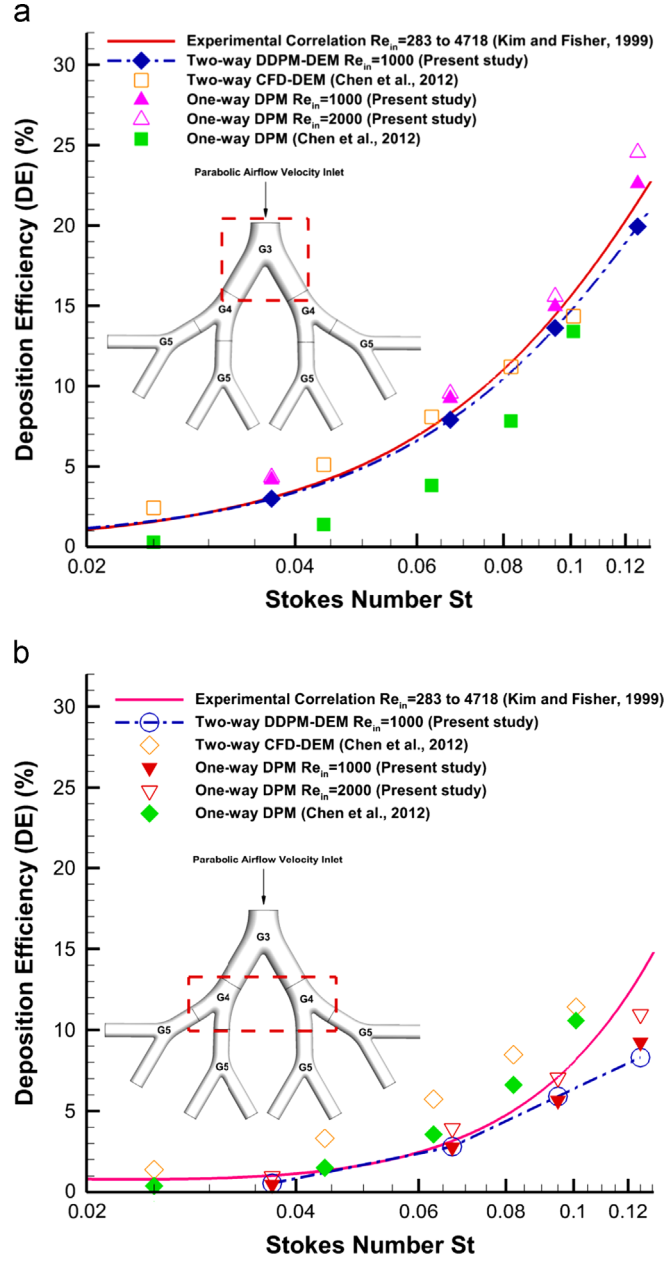
Fig. 4. Comparisons between computational data using different numerical methods and measured particle deposition efficiency correlations (Kim & Fisher, 1999): (a) for the first bifurcation (G3); (b) for the second bifurcations (G4).

4. Results and discussion

Employing two-way DDPM–DEM, one-way DPM and two-way DPM, dilute and dense particulate suspensions in different triple bifurcating lung airway geometries (i.e., G3–G6, G6–G9, and G9–G12) were simulated. Of interest is physical insight of particle transport patterns and the resulting deposition efficiencies determined by interactions between particles and airflows when using DDPM–DEM compared to DPMs. The particle diameter is from 4 μm to 10 μm. The particle density varies with the Stokes number, which varies from 0.037 to 0.125. The particulate volume fraction of the initial particle distribution ranges from 2% to 30%. The initial particle velocity was assumed to be equal to the local airflow velocity. Other boundary conditions are discussed in Section 2.4.

4.1. Comparisons of total deposition efficiency predictions using DDPM–DEM Vs. DPM

Focusing on the relationship between inlet particle stacking volume fraction (PSVF) ϕ and percentage of fate changing particles (PFCP) $\Delta\beta_p$ (see Eqs. (25) and (27)), we investigated particle transport and deposition in different bifurcating
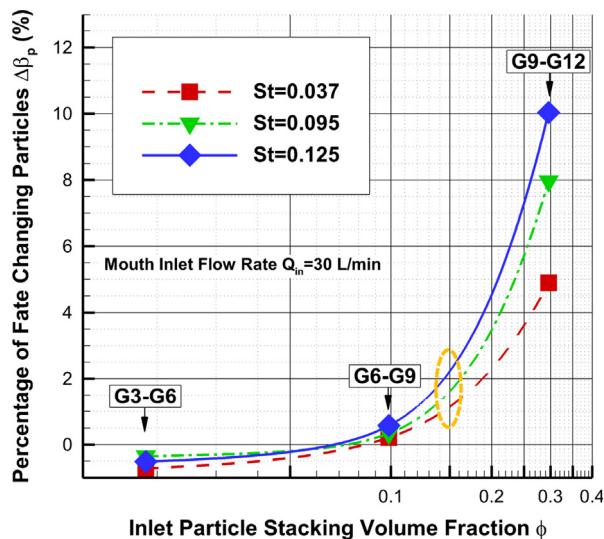
Fig. 5. Percentage of fate changing particles $\Delta\beta_p$ vs. inlet particle stacking volume fraction ϕ in bifurcating airways with different generations for a mouth inlet flow rate of $Q_{in}=30$ L/min.

generations with the inlet velocities derived from the same mouth-inlet flow rate, i.e., 30 L/min. The relationship between $\Delta\beta_p$ and ϕ under the same mouth-inlet flow rate condition is more instructive for the guidance of choosing different methods. Additionally, the M_{layer} is assumed to be equal to 1. The relationship between the PFCP, $\Delta\beta_p$, and PSVF, ϕ, in triple bifurcating airways with different generations under the mouth inlet flow rate $Q_{in}=30$ L/min is shown in Fig. 5.

In terms of deposition efficiency predictions for micron particles in the idealized lung airways, it is evident that using just DPM may very slightly over-predict the DEs from G3 to G6 and significantly under-predict the DEs from G6–G9 and G9–G12. It demonstrates that particle–particle interactions must be considered for accurate DE predictions when $\phi > 0.1$. Specifically, with the increase in ϕ from G3–G6 to G9–G12, $\Delta\beta_p$ increases as well, indicating that the influence of particle–particle interaction on the particle deposition efficiency becomes stronger. Furthermore, in G6–G9 and G9–G12 with the increase in Stokes number, $\Delta\beta_p$ also increases. As mentioned, the reason is that at higher Stokes numbers more particles will be influenced by the particle–particle interactions, requiring the use of DDPM–DEM. As a quantitative example, assuming that DDPM–DEM becomes necessary when $\Delta\beta_p$ is larger than 1%, it can be observed from Fig. 5 that when the inlet particle stacking volume fraction is larger than, say, 15%, $\Delta\beta_p$ is larger than 1% (see the orange dashed line circle in Fig. 5). It should be noted that for particle transport and deposition with other inlet and initial conditions in human lung airways, model combination criteria may vary.

4.2. Comparisons of regional deposition efficiency predictions using DDPM–DEM Vs. DPM

Setting St=0.125 as an example, regional deposition efficiency (RDE) comparisons, using DDPM–DEM vs. one-way DPM in G6–G9 and G9–G12, are shown in Fig. 6(a) and (b). The major predictive DE differences occur in the first bifurcations of both geometries. This is because of the relatively high particulate volume fractions, indicating a stronger influence of particle–particle interaction on particle deposition patterns. Although the local particulate volume fraction will be reduced as the particles move downstream, larger differences can still be observed in the 2nd bifurcation of G9–G12 rather than in G6–G9; again, in part due to particle–particle interactions. Also, one-way DPM provides higher DE than DDPM–DEM in the third bifurcations, both in G6–G9 and G9–G12. Such a phenomenon is probably due to the particle–particle interactions which allows depositing particles to re-suspend into the airway stream and hence migrate to deeper lung regions. In the third bifurcations of G9–G12, particles deposit more evenly in different branches rather than in G6–G9. This is because of the dominant viscous airflow effect in higher (smaller) generations, while primary particle impaction at lower airflow velocities is of little importance. Based on the RDE prediction differences using DDPM–DEM vs. DPM, it can be concluded that the DDPM–DEM approach provides extensive particle transport and interaction simulation results, which makes this methodology more realistic than just using DPM.

4.3. Particle dynamics in triple bifurcation units

Compared with one-way DPM, the fully-coupled DDPM–DEM can provide three-dimensional particle dynamics in different triple bifurcation airways over time. Snapshots of particle distributions in G6–G9 bifurcating lung airways at St=0.125 and a mouth inlet flow rate of $Q_{in}=30$ L/min are shown in Fig. 7(a)–(i) demonstrate air–particle and particle–particle interactions.
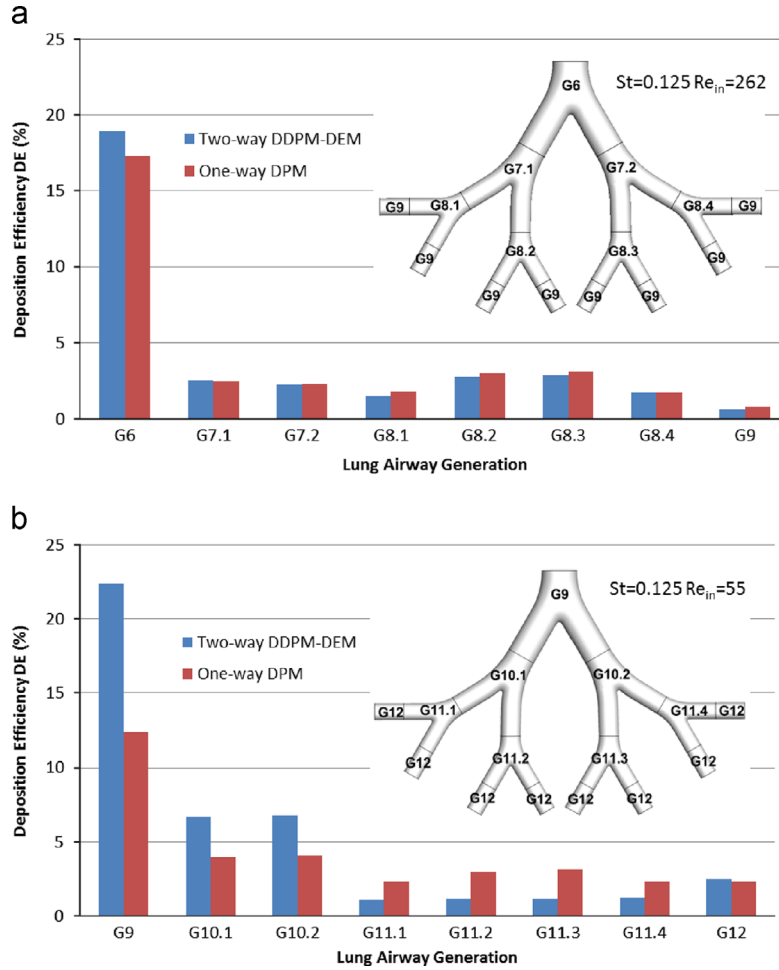
Fig. 6. Local particle deposition efficiency comparisons using different numerical methods in different triple bifurcating lung airways with mouth inlet flow rate $Q_{in}=30$ L/min (a) G6–G9 (b) G9–G12.

In order to depict the particle transport dynamics, 10,000 random-parabolic distributed particles with $d_p=10$ μm were released at $t=0$ s. At $t=0.0002$ s (see Fig. 7(a)), the particle cloud appears as a paraboloid due to the convection of the parabolic air velocity profile. As marked by the red dashed line in Fig. 7(a), some particles obtained extra momentum during the particle–particle collisions, overshooting the paraboloidal frontier of the particle cloud. At $t=0.0015$ s, the mainstream of the particle cloud impacts the first bifurcation point (carinal ridge) and intense particle–particle interactions occur near the divider (see the black dashed circle in Fig. 7(b)). From $t=0.0015$ s to 0.0035 s, due to the skewed secondary flows (Feng, 2013), the particle cloud splits and splashes downstream into the daughter tubes (see Fig. 7(c)). At $t=0.0060$ s, with particles entering the third bifurcation, some particles are still in G6, moving with lower velocities. Those particles are marked inside the red dashed ellipse near the inlet in Fig. 7(d). At $t=0.0085$ s, the frontier of the particle cloud, which just has reached G8.1 (see Fig. 7(e)), splits due to the secondary flow effect. Such a phenomenon can be also observed in the parent tube of G8.4. From $t=0.0120$ s to 0.0500 s (see Fig. 7(f)–(i)), the initial particle cloud gradually spreads downstream and is distributed throughout the entire bifurcating airways. At $t=0.0500$ s (see Fig. 7(i)) more than 90% of the particles escaped or deposited in the bifurcating airways, while the rest are particles near the wall, moving slowly. At $t=0.0935$ s, less than 1% of the injected particles are still moving in G6–G9, which indicates the formation of the particle deposition pattern. As the particles travel towards the outlets, the particulate volume fraction will become lower. Hence, quite similar transport characteristics can be observed when compared to using only DPM.

4.4. Particle deposition mechanisms and local deposition efficiencies

Figure 8(a)–(d) show the local particle deposition patterns in G6–G9 and G9–G12 at different Stokes numbers and inlet Reynolds numbers. For values higher than St=0.125 or Re_{in}=262, the concentrated particle deposition near bifurcating points demonstrate that direct impaction is the dominant deposition mechanism. Meanwhile, for values lower than St=0.037 or Re_{in}=55, the local secondary flow effect and particle–particle interaction effect become significant, leading to

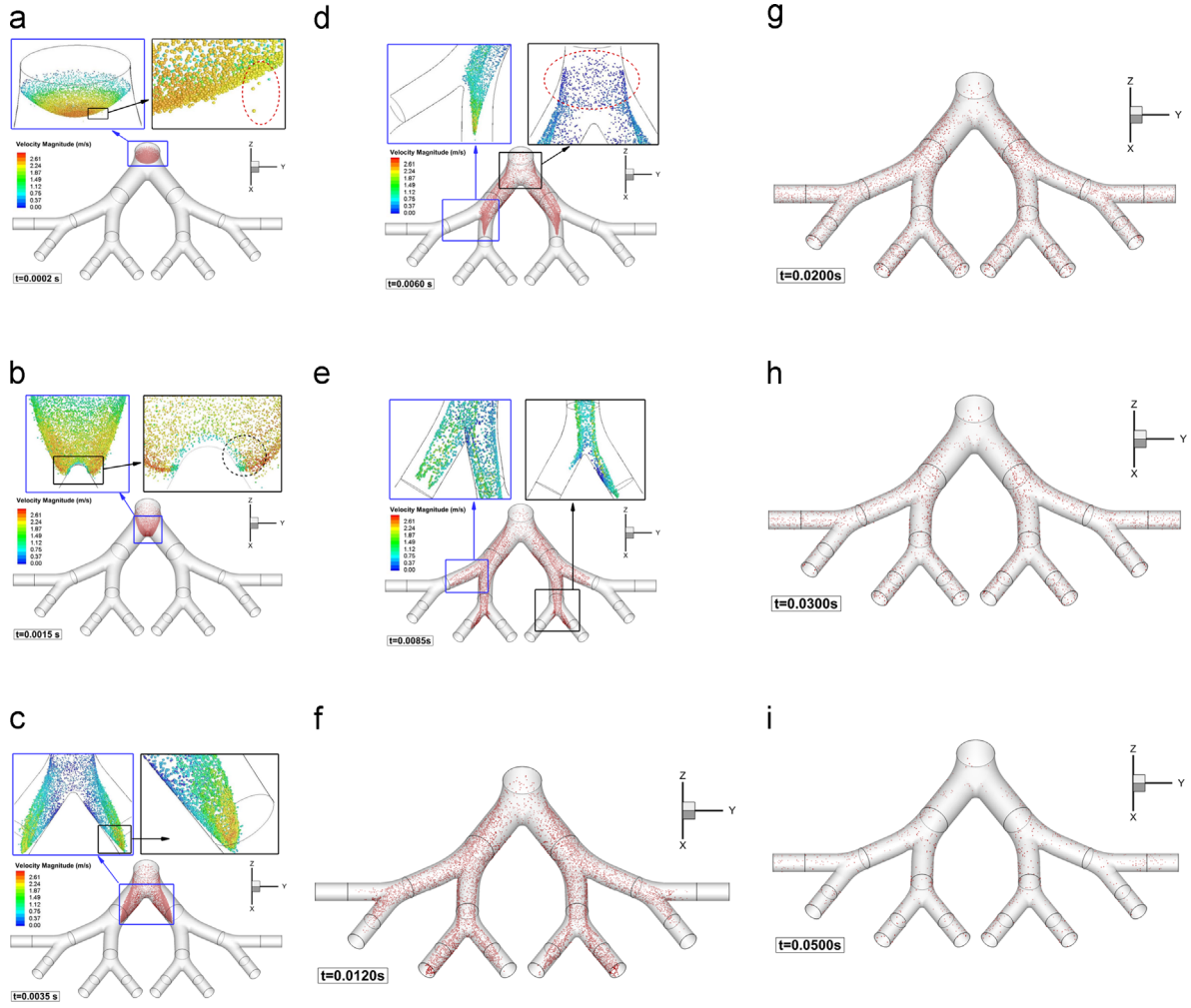**Fig. 7.** Time evolution for volumetric particle pulse in G6–G9 bifurcating lung airway for St=0.125, Q_{in}=30 L/min, and d_p=10 μm: (a) t=0.0002 s; (b) t=0.0015 s; (c) t=0.0035 s; (d) t=0.0060 s; (e) t=0.0085 s; (f) t=0.0120 s; (g) t=0.0200 s; (h) t=0.0300 s; (i) t=0.0500 s. (For interpretation of the references to color in this figure, the reader is referred to the web version of this article.)

more evenly distributed particle deposition patterns. Combined with the particle transport discussed in Section 4.3, the major particle deposition mechanisms in bifurcating lung airways from G3 to G12 can be summarized as follows:

(1) deposition near bifurcating points due to direct inertial impaction;
(2) wall deposition due to 3-D secondary flow effects; and
(3) wall deposition due to particle–particle (elastic) contact forces.

The local deposition patterns vary among cases with different St and Re_{in} combinations (see Fig. 8(a)–(d)). Although the differences in total deposition efficiency are not noticeable between Re_{in}=55 and 262 at the same Stokes numbers (e.g., St=0.037 and 0.125), the local deposition patterns of the two groups differ from each other. For example, at Re_{in}=55 particles deposit more evenly in both G6–G9 and G9–G12. In contrast, depositing particles at Re_{in}=262 are more concentrated at bifurcating points due to the stronger inertial impaction effect.

4.5. Parametric impacts on particle deposition efficiencies in different triple bifurcation units

While Fig. 8(a)–(d) show the local particle deposition patterns for different St and Re_{in} numbers, Fig. 9 depicts the total deposition efficiency (TDE) as a function of Stokes number and inlet Reynolds number in G3–G6, G6–G9, and G9–G12. In fact, TDE is an exponential function of the Stokes number because more particles deposit due to the stronger direct inertial impact effect. Given a Stokes number, the TDE data in Fig. 9 indicate that Re_{in} has a minor effect. This was also observed by Kim & Fisher (1999) as well as Zhang & Kleinstreuer (2001). Nevertheless, higher Re_{in} values indicate stronger direct impaction, thereby leading to elevated TDEs.
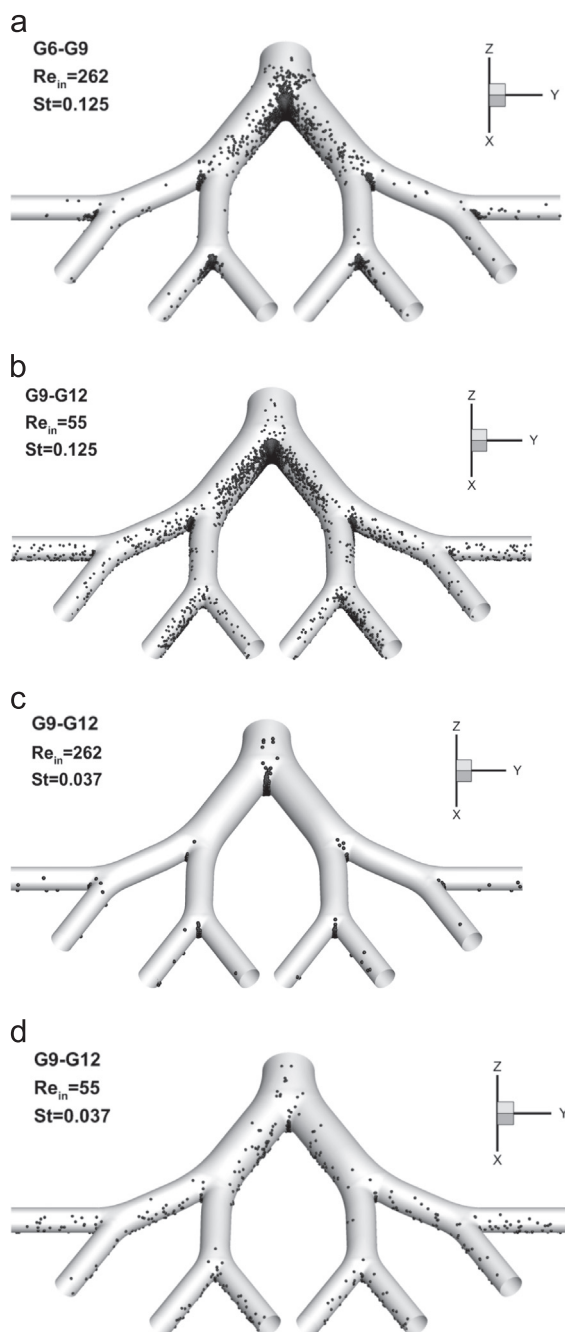
Fig. 8. Local particle deposition patterns in different bifurcating airways: (a) in G6-G9 at $Re_{in}=262$ and $St=0.125$; (b) in G9–G12 at $Re_{in}=55$ and $St=0.125$; (c) in G6–G9 at $Re_{in}=262$ and $St=0.037$; (d) in G9–G12 at $Re_{in}=55$ and $St=0.037$.

4.6. Limitations of the study

Presently steady-state inlet conditions were assumed, based on 30 L/min and 60 L/min inhalation flow rates at the mouth, and using the morphology of idealized lung airways (Weibel, 1963). Limited by the intense computational cost of DDPM–DEM, simulation of dense suspensions of micro/nanoparticles in the whole human respiratory system would be quite taxing. However, for a more comprehensive application using DDPM–DEM, simulations should be extended from the current triple bifurcating airway segments (e.g., G3–G6, G6–G9, and G9–G12) to the entire human respiratory systems, i.e., from the nose/oral cavities to the alveolar region (see Kolanjiyil & Kleinstreuer, 2013a, b). Also, limited by the availability of experimental data, particle interaction mechanisms and properties can only be approximated via the current contact models. Specifically for particle transport in lung airways, measured parameter values for the particle–particle contact
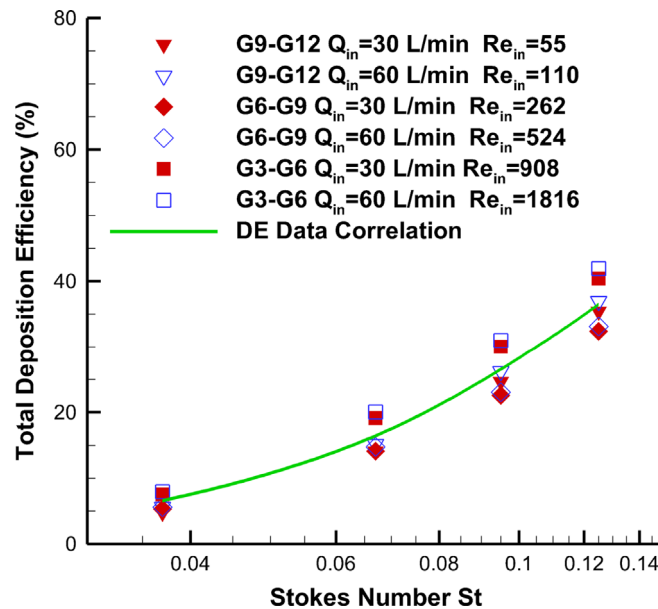
Fig. 9. The total deposition efficiencies in bifurcating airways with different mouth inlet flow rates, inlet Reynolds numbers, and Stokes numbers.

models, i.e., stiffness coefficient, frictional coefficient, damping coefficient and restitution coefficient, should be obtained (Mader & Tomas, 2012). Furthermore, for the fluid–particle interacting forces and torques, empirical correlations are still required.

5. Summary

In this study, the validity and necessity of DDPM–DEM for dilute and dense particle suspension transport and deposition in different lung airway bifurcations, i.e., G3–G6, G6–G9, and G9–G12, have been numerically investigated. A new condition for CF–PD model combination in terms of a relationship between inlet particle stacking volume fraction, ϕ, and percentage of fate changing particles, $\Delta\beta_p$, is proposed. It can be concluded that DDPM–DEM is a more accurate CF–PD model than DPM at elevated ϕ-values and Stokes numbers, allowing now to simulate particle–particle and particle–wall interactions. However, to assure numerical stability and accuracy more stringent computational requirements have to be considered when introducing additional parameters and coupling via DDPM–DEM. Although the computational cost is quite high for large-scale system simulations, DDPM–DEM is promising to be the next-generation CF–PD modeling approach for solving lung dynamic problems for dense inhaled aerosol suspensions. New physical insight to the fluid–particle dynamics in bifurcating airways has been provided as well.

Future research will focus on parallel computational efficiency enhancement of DDPM–DEM, development of a combined CF–PD model with particle–particle and particle–wall interactions for micron as well as nanoparticles, and applications to the whole human respiratory system.

Acknowledgments

References

Aljuri, N., Venegas, J.G., Nair, A., Perkins, R.C. (2012). *U.S. Patent No. 8,137,302*. Washington, DC: U.S. Patent and Trademark Office.
Alobaid, F., Ströhle, J., & Epple, B. (2012). Extended CFD/DEM model for the simulation of circulating fluidized bed. *Advanced Powder Technology, 24*(1), 403–415.
Armstrong, B., & de Wit, C.C. (1996). Friction modeling and compensation. *The Control Handbook, 77*, 1369–1382.
Chen, X., Zhong, W., Zhou, X., Jin, B., & Sun, B. (2012). CFD–DEM simulation of particle transport and deposition in pulmonary airway. *Powder Technology, 228*, 309–318.
Comer, J.K., Kleinstreuer, C., Hyun, S., & Kim, C.S. (2000). Aerosol transport and deposition in sequentially bifurcating airways. *Journal of Biomechanical Engineering, 122*(2), 152–158.
Crowe, C.T., Schwarzkopf, J.D., Sommerfeld, M., & Tsuji, Y. (2011). *Multiphase Flows with Droplets and Particles* 2nd ed). CRC Press: Boca Raton, FL, USA.

Cui, X. (2012). CFD study of the flow field and particle dispersion and deposition in the upper human respiratory system (Ph.D. dissertation). Germany: Ruperto-Carola University of Heidelberg.

Cundall, P.A., & Strack, O.D.L. (1979). A discrete numerical model for granular assemblies. *Geotechnique*, *29*, 47–65.

Di Renzo, A., Cello, F., & Di Maio, F.P. (2011). Simulation of the layer inversion phenomenon in binary liquid–fluidized beds by DEM–CFD with a Drag Law for polydisperse systems. *Chemical Engineering Science*, *66*, 2945–2958.

Ergun, S. (1952). Fluid flow through packed columns. *Chemical Engneering Progress*, *48*, 89–94.

Feng, Y. (2013). Computational ellipsoidal particle–fluid analysis and discrete element method with applications to particle transport and deposition in human respiratory models (Ph.D. dissertation). Raleigh, NC, USA: North Carolina State University.

Hilton, J.E., & Cleary, P.W. (2011). The influence of particle shape on flow modes in pneumatic conveying. *Chemical Engineering Science*, *66*(3), 231–240.

Johnson, R.W. (1998). *The Handbook of Fluid Dynamics 1st ed*). Springer-Verlag: Heidelberg, Germany.

Kafui, K.D., Thornton, C., & Adams, M.J. (2002). Discrete particle-continuum fluid modelling of gas–solid fluidized beds. *Chemical Engineering Science*, *57*, 2395–2410.

Kim, C.S., & Fisher, D.M. (1999). Deposition characteristics of aerosol particles in sequentially bifurcating airway models. *Aerosol Science & Technology*, *31*(2–3), 198–220.

Kleinstreuer, C., Zhang, Z., & Donohue, J.F. (2008). Targeted Drug-Aerosol Delivery in the Human respiratory System. *Annual Review of Biomedical Engineering*, *10*, 195–220.

Kleinstreuer, C., & Feng, Y. (2013). Lung deposition analyses of inhaled toxic aerosols in conventional and less harmful cigarette smoke: a review. *International Journal of Environmental Research and Public Health*, *10*(9), 4454–4485.

Kolanjiyil, A.V., & Kleinstreuer, C. (2013a). Nanoparticle mass transfer from lung airways to systemic regions - Part I: whole-lung aerosol dynamics. *Journal of Biomechanical Engineering*, *135*(12). (No. 121003-1–121003-11).

Kolanjiyil, A.V., & Kleinstreuer, C. (2013b). Nanoparticle mass transfer from lung airways to systemic regions—Part II: multi-compartment modeling. *Journal of Biomechanical Engineering135*(12). (121004-1–121004-12).

Li, H., Li, Y., Gao, F., Zhao, Z., & Xu, L. (2012). CFD–DEM simulation of material motion in air-and-screen cleaning device. *Computers and Electronics in Agriculture*, *88*, 111–119.

Loth, E. (2008). *Computational Fluid Dynamics of Bubbles, Drops and Particles*. Cambridge University Press: Cambridge, UK.

Mader, K., & Tomas, J. (2012). Modeling of the contact behaviour between fine adhesive particles with viscous damping. In C.Y. Wu (Ed.), *Discrete Element Modelling of Particulate Media*, *339*. The Royal Society of Chemistry: Cambridge, UK, pp. 89–112.

Neuwirth, J., Antonyuk, S., Heinrich, S., & Jacob, M. (2012). CFD–DEM study and direct measurement of the granular flow in a rotor granulator. *Chemical Engineering Science*, *86*, 151–163.

O'Sullivan, C., & Bray, J.D. (2004). Selecting a suitable time step for discrete element simulations that use the central difference time integration scheme. *Engineering Computations*, *21*, 278–303.

Raji, A.O. (1999). Discrete element modelling of the deformation of bulk agricultural particulates (Doctoral dissertation). UK: University of Newcastle upon Tyne.

Ren, B., Zhong, W., Jin, B., Yuan, Z., & Lu, Y. (2011). Modeling of gas–particle turbulent flow in spout-fluid bed by computational fluid dynamics with Discrete Element Method. *Chemical Engineering & Technology*, *34*(12), 2059–2068.

Tong, Z.B., Yang, R.Y., Chu, K.W., Yu, A.B., Adi, S., & Chan, H.K. (2010). Numerical study of the effects of particle size and polydispersity on the agglomerate dispersion in a cyclonic flow. *Chemical Engineering Journal*, *164*(2), 432–441.

Tong, Z.B., Zheng, B., Yang, R.Y., Yu, A.B., & Chan, H.K. (2012). CFD–DEM investigation of the dispersion mechanisms in commercial dry powder inhalers. *Powder Technology*, *240*, 19–24.

Tsuji, Y., Kawaguchi, T., & Tanaka, T. (1993). Discrete particle simulation of 2-dimensional fluidized-bed. *Powder Technology*, *77*, 79–87.

Tsuji, Y., Tanaka, T., & Ishida, T. (1992). Lagrangian numerical simulation of plug flow of cohesionless particles in a horizontal pipe. *Powder Technology*, *71*(3), 239–250.

Van der Hoef, M.A., van Sint Annaland, M., Deen, N.G., & Kuipers, J.A.M. (2008). Numerical simulation of dense gas–solid fluidized beds: a multiscale modeling strategy. *Annual Review of Fluid Mechanics*, *40*, 47–70.

Wang, G.Q., Hao, W.J., & Wang, J.X. (2010). *Discrete Element Method and Its Application using EDEM*. Northwestern Polytechnical University Press: Xi'an, China.

Weibel, E.R. (1963). *Morphometry of the Human Lung*. Academic Press: New York, NY, USA.

Wen, Y.C., & Yu, Y.H. (1966). Mechanics of fluidization. *Chemical Engineering Progress Symposium Series*, *62*, 100–111.

Wong, W., Fletcher, D.F., Traini, D., Chan, H.K., & Young, P.M. (2012). The use of computational approaches in inhaler development. *Advanced drug delivery reviews*, *64*(4), 312–322.

Zhang, Z., & Kleinstreuer, C. (2001). Effect of particle inlet distribution on deposition in a triple bifurcation lung airway model. *Journal of Aerosol Medicine*, *14*(1), 13–29.